

Modeling 237 Lyman- α spectra of the MUSE-Wide survey[★]

Max Gronke

Institute of Theoretical Astrophysics, University of Oslo, Postboks 1029, 0315 Oslo, Norway
e-mail: maxbg@astro.uio.no

Received 17 August 2017/Accepted 20 September 2017

ABSTRACT

We compare 237 Lyman- α ($Ly\alpha$) spectra of the MUSE-Wide survey to a suite of radiative transfer simulations consisting of a central luminous source within a concentric, moving shell of neutral gas, and dust. This six parameter shell-model has been used numerous times in previous studies, however, on significantly smaller data-sets. We find that the shell-model can reproduce the observed spectral shape very well – better than the also common “Gaussian-minus-Gaussian” model which we also fitted to the dataset. Specifically, we find that $\sim 94\%$ of the fits possess a goodness-of-fit value of $p(\chi^2) > 0.1$. The large number of spectra allows us to robustly characterize the shell-model parameter range, and consequently, the spectral shapes typical for realistic spectra. We find that the vast majority of the $Ly\alpha$ spectral shapes require an outflow and only $\sim 5\%$ are well-fitted through an inflowing shell. In addition, we find $\sim 46\%$ of the spectra to be consistent with a neutral hydrogen column density $< 10^{17} \text{ cm}^{-2}$ – suggestive of a non-negligible fraction of continuum leakers in the MUSE-Wide sample. Furthermore, we correlate the spectral against the $Ly\alpha$ halo properties against each other but do not find any strong correlation.

Key words. radiative transfer – line: formation – line: profiles – galaxies: high-redshift – scattering

1. Introduction

Not many branches of astrophysics show a similar fast transition from theory- to data-driven as the study of the high- z Universe through Lyman- α ($Ly\alpha$) emitting objects. While predicted already half a century ago (Partridge & Peebles 1967), the first detections of high-redshift $Ly\alpha$ emitters was not until more than 25 years later (e.g., Møller & Warren 1993; Rhoads et al. 2000). They were thus preceded by groundbreaking theoretical studies – which still represent the solid foundation of our understanding of $Ly\alpha$ radiative transfer in astrophysical environments today (Osterbrock 1962; Adams 1972; Neufeld 1990). These theoretical studies were often accompanied by numerical radiative transfer codes (e.g., Adams 1972; Bonilha et al. 1979) – with the focus shifting towards the latter more recently (e.g., Dijkstra et al. 2006; Verhamme et al. 2006; Hansen & Oh 2006). While this numerical work together with increased computational power allowed for the study of more complex geometries (such as the output from hydrodynamical simulations) as well as the consideration of a wider parameter space, the predictive power has naturally decreased due to this multiplication of degrees of freedom and the associated degeneracies.

In addition to these difficulties, a somewhat unfortunate incident arguably slowed down the progress on theoretical side considerably, namely the apparent non-requirement for (more) complex theoretical models in order to explain a wide range of observed $Ly\alpha$ spectra. Specifically, a homogeneous shell of neutral hydrogen (and dust) surrounding a $Ly\alpha$ and continuum emitting source (as first advocated by Ahn et al. 2003) seems to be able to reproduce many observed line shapes from $z \sim 0$ (Yang et al. 2017) to higher redshifts (Verhamme et al. 2008; Karman et al. 2017). This has been shown using large libraries of pre-computed line shapes

(Schaerer et al. 2011; Gronke et al. 2015) which can be compared to observations. In spite of this automatizing of the fitting procedure and the consequent common usage of the “shell model”, the physical meaning of its parameters is still unclear. Also, the structure of the shell-model, that is, the existence of a large solid shell of cold, neutral gas seems somewhat contrived. Nevertheless, the shell-model has been studied numerous times and the effect of its parameters on the spectral shape are understood well (Verhamme et al. 2015). These facts make the shell-model a common starting point of theoretical modeling of $Ly\alpha$ propagation – and it does so since more than a decade.

This rather slow progress on the theoretical side has not halted the planning and execution of new experiments geared towards $Ly\alpha$ detection and study. As a result, the pure number of detected $Ly\alpha$ emitting objects – even at the highest observable redshifts – has increased impressively (e.g., the latest detection of ~ 2000 $Ly\alpha$ emitters at $z \sim 6-7$, Ouchi et al. 2017; also see Barnes et al. 2014, for a list of $Ly\alpha$ surveys), and the quality of the detections has improved significantly (e.g., McGreer et al. 2017). This development has not only led to the discovery of new types of astrophysical objects such as “Lyman- α blobs” (e.g., Francis et al. 1996; Fynbo et al. 1999; Steidel et al. 2000; North et al. 2017), “giant $Ly\alpha$ halos” (e.g., Cantalupo et al. 2014; Hennawi et al. 2015; Cai et al. 2016), and “extreme equivalent width objects” (e.g., Sobral et al. 2015) but also opened up the chance of statistical usage of $Ly\alpha$ data, for example, to constrain the “Epoch of Reionization” (see review by Dijkstra 2014) or the leakage of ionizing photons (e.g., Dijkstra et al. 2016b; Verhamme et al. 2017).

The latest stage in this series of technological advances and consequent observational progress has been the implementation of ESO’s “Multi Unit Spectroscopic Explorer” (MUSE; Bacon et al. 2010). Equipped with 24 integral field units, this integral field spectrograph has literally added an additional dimension to $Ly\alpha$ observations and will thus multiply the available $Ly\alpha$ data even further. The unprecedented sensitivity of MUSE

[★] The full Table A.1 is only available at the CDS via anonymous ftp to cdsarc.u-strasbg.fr (130.79.128.5) or via <http://cdsarc.u-strasbg.fr/viz-bin/qcat?J/A+A/608/A139>

has already revealed the ubiquity of Ly α emission throughout the Universe (Bacon et al. 2015; Wisotzki et al. 2016; Drake et al. 2017), and the combination of imaging with spectral information opens up many new possibilities for Ly α data analysis – which will further our understanding of astrophysical Ly α emitting objects.

Recently, the data of the first installment of the MUSE-Wide survey has been released publicly (Herenz et al. 2017) which contains 237 Ly α spectra around $z \sim 4$. The sample (corresponding to $\sim 20\%$ of the final survey area) is emission line-selected which allows an unbiased spectral analysis. We take this opportunity to assemble a statistical relevant sample of shell-model fits. Thus far, the number of modeled spectra found in the literature are often merely individual spectra (e.g. Vanzella et al. 2016; Dahle et al. 2016) or compilations up to ~ 10 s (Hashimoto et al. 2015; Karman et al. 2017; Yang et al. 2017). A (much) greater number of spectra will, thus, allow us to address the following questions:

- How well can the shell-model reproduce observed spectral line shapes? Is there, e.g., a certain spectral characteristic that cannot be reproduced?
- What are common values for shell-model parameters? Answering this question is useful for studies concerned with a single object and might help them to characterize how unusual their spectral shape is.
- Do any correlations amongst the shell-model or with external parameters exist?

Furthermore, this work will provide the foundational data for future work “decrypting” the shell-model parameters. In a recent series of papers (Gronke & Dijkstra 2016; Gronke et al. 2016; Gronke et al. 2017), we’ve shown already that the shell-model parameters do not reflect the physical properties of a simple multiphase model. However, in such a case the spectra do commonly also show more flux a line-center and are less asymmetric (in spite of outflows) compared to observed line-profiles. However, in the presence of small-scale structure such as tiny “cloudlets” (as theoretically predicted by McCourt et al. 2016), Ly α photons escape the – still multiphase – system as it was homogeneous which yields more realistic spectra, and makes the obtained shell-model parameters physically meaningful. In this work, we will interpret the data also in the light of these recent results.

The paper is structured as follows: Sect. 2 describes the MUSE-Widefield data set, and the fitting procedure. We present and discuss our results in Sect. 3, and conclude in Sect. 4. When required, we use the Planck Collaboration et al. (2016) parameters of a flat Λ CDM Universe ($H_0 = 67.7 \text{ km s}^{-1} \text{ Mpc}^{-1}$, $\Omega_{\text{m}0} = 0.307$, $\Omega_{\Lambda 0} = 0.691$), and use “log” as logarithm with base ten.

2. Method

2.1. The MUSE-Wide data

The MUSE-Wide catalogue used in this work was described extensively in Herenz et al. (2017). Here, we summarize the main properties of the data set and explain which pre-processing steps we undertook prior to modeling.

In total, the catalogue contains 831 datasets with a spectral resolution of 2.5 Å out of which 237 contain a Ly α line. These Ly α emitting objects are in a redshift range of $z_{\text{MW}} = [2.97, 6.00]$ with a median redshift of 3.83. The redshift z_{MW} given for these objects stems from fitting an asymmetric profile

to the Ly α line (see Sect. 3.4.1 in Herenz et al. 2017) in order to obtain the peak wavelength which was converted to a redshift. The quoted redshift error is due to the fitting procedure, i.e., corresponds to an uncertainty in the peak position. This means for both, the redshift and the redshift error, no correction for radiative transfer effects was introduced. During the fitting procedure, we will leave the redshift as a free parameter. In order to use the spectra, we extract a wavelength range which allows for a shift of $\Delta z = [-0.02, 0.01]$ from the given peak-redshift while considering that even with a maximum shift no data point is outside the range of $[\pm 2500 \text{ km s}^{-1}]$ which is supported by the fitting pipeline. The asymmetric Δz range is due to the fact that most Ly α peaks are redwards of non-resonant lines, i.e., we expect in most cases a z value blueward of z_{MW} (i.e., $z < z_{\text{MW}}$). However, we still leave enough room ($\Delta z = 0.01$ corresponds to $\sim 750 \text{ km s}^{-1}$ at $z = 3$ – a value larger than commonly found shifts of several $\sim 100 \text{ km s}^{-1}$, Shapley et al. 2003; Steidel et al. 2010; Kulas et al. 2012) for an opposite shift. This procedure ensures that even while shifted the same number of data points is compared to the theoretical spectrum.

As some spectral data contain negative mean continuum fluxes – which are unphysical – we take a conservative approach, and remove this continuum level from all the spectra. This implies, that we will only use the Ly α line shape to fit theoretical spectra to it and ignore the surrounding continuum.

Another important property of the Herenz et al. (2017) dataset used in this work include the “confidence” category which can be either 3 for spectra which are almost certainly Ly α ($\sim 40\%$ of the spectra), 2 for near-certainty ($\sim 52\%$), and 1 for unsure detections which are, however, not spurious ($\sim 8\%$). We refer to Herenz et al. (2017) for more details about the classification.

2.2. Shell-model fitting

The shell-model fits were carried out via an improved version of the fitting procedure described in Gronke et al. (2015). Because the shell-model consists of a central source emitting Ly α photons inside a moving shell of neutral hydrogen and dust, it can be parametrized through the HI column density N_{HI} , the (all-absorbing) dust optical depth τ_{d} , the outflow velocity v_{exp} (< 0 for infall), the intrinsic width of the Ly α line σ_{i} , and the effective temperature of the gas T .

In order to fit observed spectra by this model, one usually divides these parameters into sets of discrete and continuous ones. While the parameter space spanned by the discrete ones has to be covered through (computationally relatively expensive) radiative transfer simulations, the continuous ones can be modeled in post-processing. We model the effect of σ_{i} and τ_{d} through individual weighting of photon packages (see Gronke et al. 2015, for details) with an allowed range of $\sigma_{\text{i}} \in [1, 800] \text{ km s}^{-1}$ and $\tau_{\text{d}} \in [0, 5]$. The remaining subspace spanned by $(v_{\text{exp}}, \log N_{\text{HI}}/\text{cm}^{-2}, \log T/\text{K})$ we cover via a (54, 30, 8)-grid which totals 12 960 discrete models. Each of the models was carried out using 20 000 “Ly α ” photons with Gaussian intrinsic spectrum centered at 0 and a standard deviation of 800 km s^{-1} and 150 000 “UV” photons with uniform intrinsic spectrum in the range $\pm 2700 \text{ km s}^{-1}$.

While the parameters $\log N_{\text{HI}}/\text{cm}^{-2}$ and $\log T/\text{K}$ are spaced uniformly between their respective limits [16, 21.8] and [3, 5.8], the outflow velocity v_{exp} can take the additional values of 2 km s^{-1} , 5 km s^{-1} , and 8 km s^{-1} apart from the values with 10 km s^{-1} separation between 0 and 490 km s^{-1} . This is due

to the strong effects small velocities can have on the resulting spectrum due to the peaked nature of the Ly α scattering cross-section. Furthermore, we use the symmetry of Ly α radiative transfer to cover inflow velocities (Dijkstra 2017).

In summary, the following steps were carried out for each spectrum:

1. We fix a redshift prior of with mean $z_{\text{MW}} - 0.005$ and standard deviation of $\sigma_z = 0.005$. As stated above, the offset is due to the more likely observation of the red peak of the Ly α line. This prior is very wide and easily overruled by the data.
2. Due to the multi-modal nature of the likelihood landscape – with many local peaks which are, however, of dramatically different altitude – it is crucial to find the global likelihood maximum around which one can carry out the Monte-Carlo optimization. In a continuous parameter space with unknown likelihood function it is impossible to know whether or not this global maximization is successful. However, we do our best by combining a basinhopping algorithm over the discrete parameters with a local maximization over the continuous parameters. This means, we perform a basinhopping algorithm with randomly chosen starting position until no better results is obtained¹. Each step consists of a random displacement in parameter space followed by a local maximization using the robust POWELL algorithm. In order to speed up the global maximization process by reducing the memory access, we execute the basinhopping over a local maximization using only the continuous parameters (z , τ_d , σ_i). For this process, we use the COBYLA method (Powell 1994).
3. From this initial position, we start the affine invariant Monte-Carlo sampler emcee (Goodman & Weare 2010; Foreman-Mackey et al. 2013) with 200 walkers and 1240 steps. Specifically, we place the walkers on several positions identified through the optimization process weighted by their likelihood. In case a better-fitting spectrum ($\Delta \ln p \geq 0.5$) than the starting one is found, the MC sampling is restarted from this position (with 1200 steps).
4. For further analysis, we discard the first “burn-in” steps for which the mean (over the walkers) of each parameter does not disagree by more than 15% off the final value. From the remaining chains we compute the median values of each shell-model parameter and its uncertainties.

3. Results

3.1. Fit quality

In order to assess the quality of the shell-model fits, we computed the $p(\chi^2)$ values of the best-fit spectra. Following Pearson (1900) we compute $\chi^2 = \sum_i (y_i^{(\text{data})} - y_i^{(\text{fit})})^2 / \sigma_i^2$ (where σ_i is the flux error in bin i and the sum is taken over the N data points of the spectrum), and quote as $p(\chi^2)$ the cumulative probability of a χ^2 -distribution with N degrees of freedom having values greater than χ^2 .

Figure 1 shows the distribution of the resulting $p(\chi^2)$ values as a function of the S/N of the Ly α line. Also shown in Fig. 1 is the “confidence” class of the spectrum (as discussed in Sect. 2.1). One can notice that the $p(\chi^2)$ values are roughly uniformly distributed between the extremes of 3×10^{-13} and 0.994 with a median of 0.773. Overall, the fit quality is very good with 94% [73%] of the spectra with a $p(\chi^2) > 0.1$ [> 0.5].

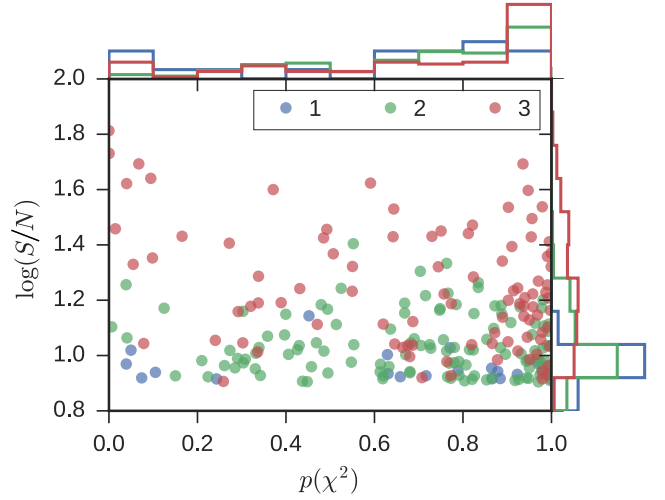


Fig. 1. Signal-to-noise ratio (S/N) of the Ly α line versus the quality of the fit ($p(\chi^2)$) computed as described in Sect. 3.1). The color coding denotes the “confidence” category as defined in Herenz et al. (2017).

As visible from Fig. 1, there seems to be no strong overall correlation neither versus the S/N (Spearman’s rank correlation coefficient of $r_s \approx -0.08$, with a two-sided p -value of a hypothesis test to check whether the two variables are correlated $p_S \approx 0.24$) nor with any of the (median) shell-model parameters ($p_S > 10^{-3}$) – with the exception of σ_i where $r_s \approx -0.26$ ($p_S \approx 4 \times 10^{-5}$). This tentative anti-correlation between σ_i and the shell-model fit quality might be suggestive of a stronger influence of radiative-transfer for spectra with lower σ_i .

Figure 2 shows the four worst fits, i.e., with the lowest $p(\chi^2)$ values. It is noteworthy that even for those spectra the fit does not “look that bad”, i.e., the model does not seem to fail catastrophically. The large χ^2 values in the examples shown in Fig. 2 can be attributed to slightly lower (negative) continuum on the blue side of the emission (two leftmost panels), or some (again with negative intensity) outliers (two rightmost panels). When increasing the error bars only by 10% (20%), the overall $p(\chi^2)$ increases from $0.77^{+0.20}_{-0.44}$ to $0.95^{+0.05}_{-0.22}$ ($0.99^{+0.01}_{-0.06}$)². This would not be the case if the theoretical model cannot reproduce certain features which are present in the observed spectra – such as an additional peak – and lets us conclude that overall, the shell-model seems to provide (surprisingly) good fits to all the 237 Ly α spectra.

3.2. Fitting results

Through the Monte-Carlo sampling, we obtain an estimate of the full posterior distribution which we quantify through one- and two-dimensional projections, and the 16th, 50th and 84th percentiles. Due to the large number of data points, we cannot show all the three percentiles (i.e., the median and the uncertainty on the parameters) in the same plot. Therefore, Fig. 3 shows first the uncertainty on the fitting parameters which we quantified through $\frac{1}{2}(q_{84} - q_{16})$ (where q_X it the X th percentile) as a function of the \bar{S}/N . Also, the color coding shows the “confidence” group with red the highest and blue the lowest confidence spectra. Clearly, with improved spectral quality, the fitting uncertainty reduces. For instance, in order to obtain a $\lesssim 0.5$ dex uncertainty on the column density, the S/N should be $\gtrsim 20$. However,

² Here – the same as the rest of this work – we use the notation A_c^b where A denotes the median and b (c) the difference to the 16th and 84th percentile.

¹ In practice, between ~ 120 and 350 are performed.

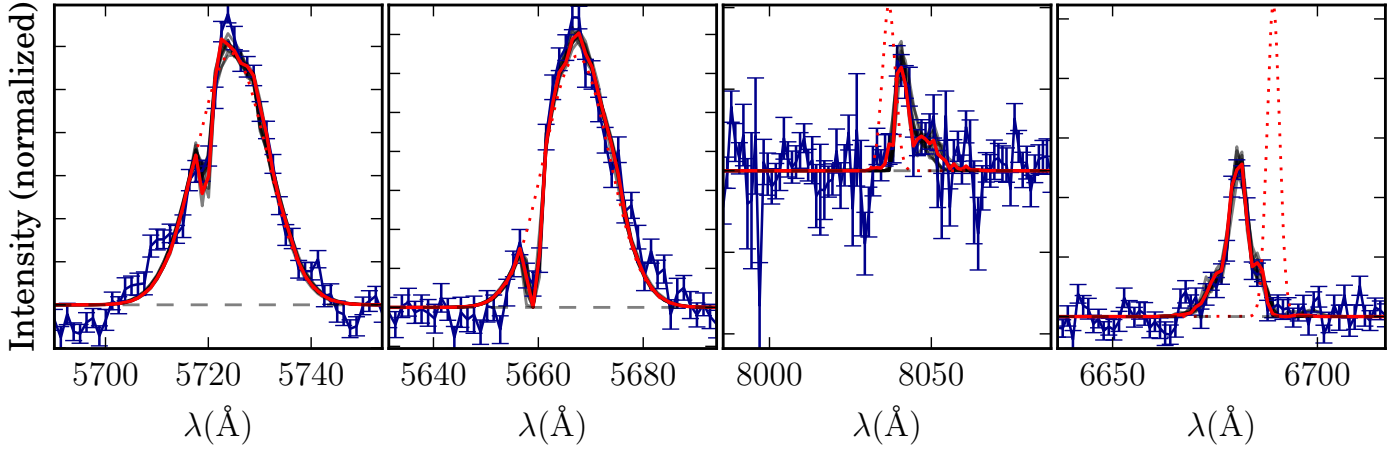


Fig. 2. The four spectra with the lowest $p(\chi^2)$ -values of (from left- to rightmost panel) $\{<0.1, 0.5, 6, 14\} \times 10^{-3}$. The data is shown in dark-blue, and the best fit shell-model spectrum with a solid red line (the dotted red line is the intrinsic spectrum). In addition, the semi-transparent black lines show 10 randomly drawn spectra from the burned-in chains. Apart from the spectrum in the third panel which has been graded with “confidence” level 2 the other three spectra have been classified as “3”.

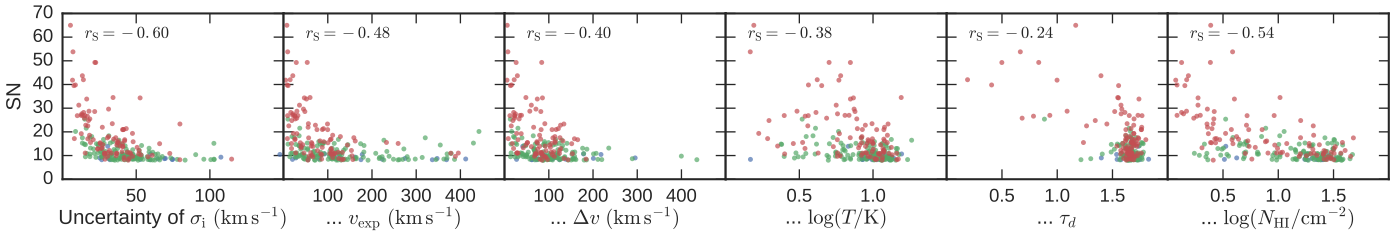


Fig. 3. Uncertainties on the obtained fitting parameters as a function of the S/N. Specifically, we show half of the 84th minus the 16th percentile of the corresponding posterior distributions. The color corresponds to the “confidence” category assigned to each spectrum by [Herenz et al. \(2017\)](#) with red for the highest confidence (3), followed by green and blue for the lowest confidence class.

as is also apparent by comparing the various panels of Fig. 3 the improvement is not equally strong for the six parameters. For instance, the dust-optical depth shows mostly (with a few exceptions) a very large uncertainty (≥ 1), and the effective temperature can only be estimated within an order of magnitude (see also [Gronke et al. 2015](#), for similar results using mock spectra).

Note that a while a greater S/N will improve the constraints on the shell-model parameters, the increased spectral resolution will – most likely – not help significantly. The MUSE spectral resolution of 2.5 \AA corresponds to a resolving power of $R \sim [1900, 3400]$ for the Ly α line in the considered redshift-range. However, above $R \sim 1000$ the uncertainty does not depend significantly on the spectral resolution (see Appendix A in [Gronke et al. 2015](#)). Better resolution spectra provide, nevertheless, important additional information as potentially features arise which cannot be captured by the shell-model (as, e.g., the extended red-wing in [McGreer et al. 2017](#); or the reversed absorption draught in [Yang et al. 2016](#)) let us peek beyond its simplicity. They might, thus, give insights into the physical meaning of the shell-model parameters³.

Figure 4 shows the one- and two-dimensional projections of the distribution of the obtained median shell-model parameters. Here, we again split the data-set according to the “confidence” group provided. No strong correlation is visible between the parameters. A slight tendency for more shift (which we show in

velocity space as Δv ; see below) for larger HI column densities or larger σ_1 are the only (weak) correlations we could identify.

The distribution of each individual parameter might help to understand what the shell-model parameters mean physically. Here we discuss them one-by-one:

- The neutral hydrogen column density is near log-normally distributed ([d’Agostino & Pearson 1973](#), test of normalization yields $p_{AP} \approx 0.14$) with mean 18.78 and standard deviation 0.88. This means the limits on this parameter are sufficiently far away, i.e., a wider covering of the parameter space would most probable not help to obtain better fits. Interestingly, $\sim 46\%$ of the spectral shapes [$\sim 36\%$ of the “category 3” spectra] are consistent (within $1-\sigma$) with a column density of $N_{\text{HI}} < 10^{17} \text{ cm}^{-2}$. This could indicate a potentially large number of Lyman-continuum leakers amongst the MUSE-Wide galaxies. However, better quality spectra are required (in particular, for the fainter galaxies) in order to draw any conclusions. With the current data set only one object clearly prefers such a low column density, that is, the 84th percentile is lower than the threshold. We would also like to caution that even if this suspicion substantiates with better quality data, i.e., also then the Ly α spectrum points towards $N_{\text{HI}} < 10^{17} \text{ cm}^{-2}$, it is not clear if these objects would be detected as continuum leakers due to a potential (non-)directional dependence of the Ly α spectrum ([Dijkstra et al. 2016a](#); Eide et al., in prep.; but see [Verhamme et al. 2012](#)).
- The “effective temperature” of the shell obtains most likely takes values of $T \sim 10^4 \text{ K}$ (median $\log(T/\text{K}) \sim 4.38$) which is close to what is expected of neutral gas. However, also

³ Naturally, if such spectral features are present they would lower the fit-quality of the shell-model discussed in Sect. 3.1. However, this has to be tested with higher-resolution data as the current data-set seems to be well fit by the shell-model.

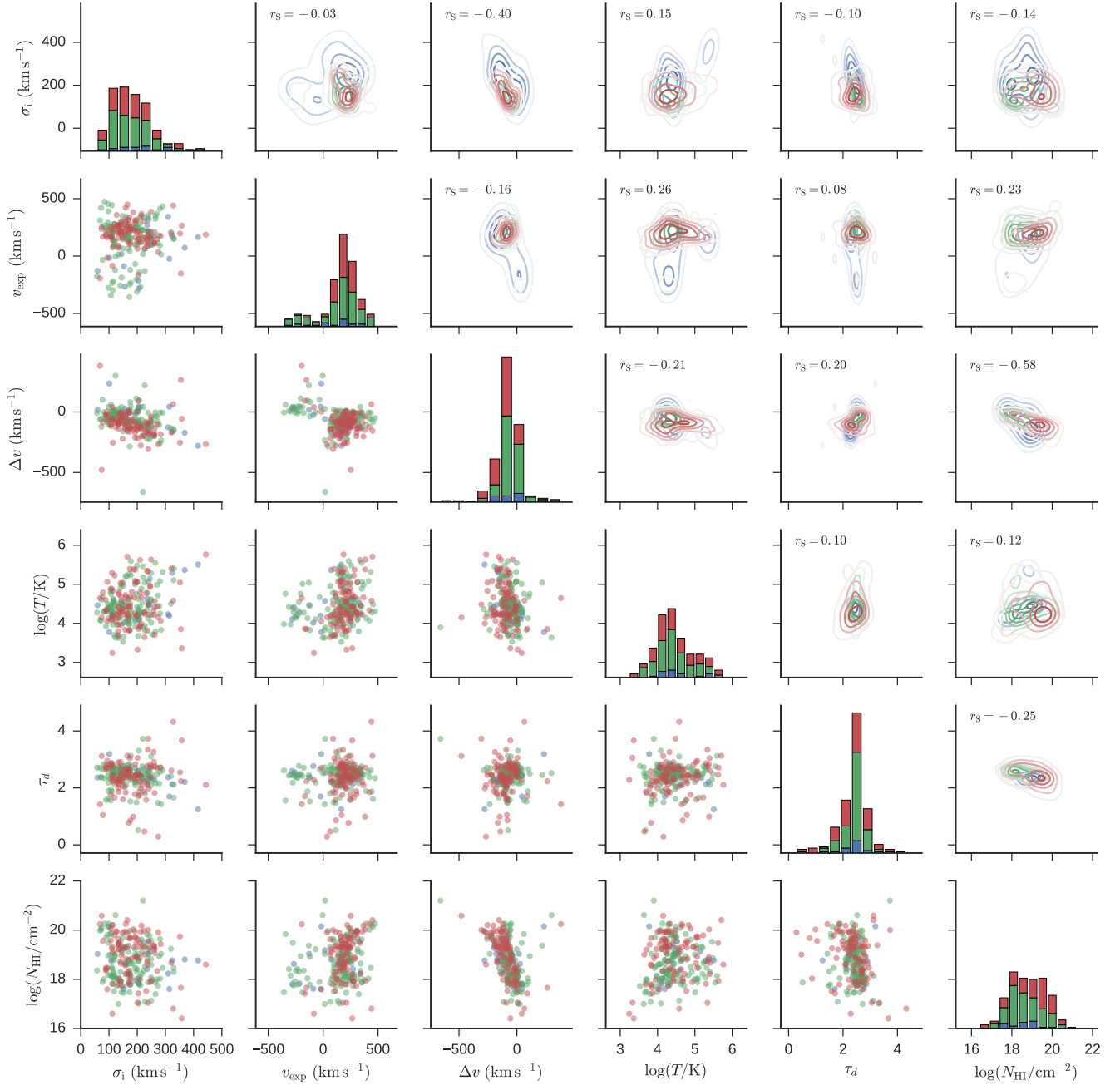


Fig. 4. Correlation matrix between the median obtained shell-model parameters. The color coding denotes the “confidence” category the spectrum was assigned (blue = 1, green = 2, red = 3). While the *lower triangle* shows scatter plots with each spectrum marked individually, the same data is plotted as contours of kernel-density estimators in the *upper right triangle*. The *panels along the diagonal* show stacked histograms of the (projected) distribution.

larger (and smaller) values are found – and, in particular temperatures of $T \sim 10^5$ K which are thermally unstable. If the shell-model temperature had some physical meaning, these values could be explained with subgrid turbulence which enters as $T_{\text{eff}} = T_0 + \langle v^2 \rangle m/k_B$, i.e., dispersion velocities of $\sqrt{\langle v^2 \rangle} \sim 25$ km s $^{-1}$ would correspond to an effective temperature of $T \sim 10^5$ K. Note also that mostly ~ 1 dex uncertainty is associated with the effective temperature (cf. Fig. 3).

- The width of the intrinsic spectrum σ_i occupies the range $\sim 172_{-60}^{+75}$ km s $^{-1}$. The distribution is furthermore faster declining towards smaller values of σ_i which makes the canonical value of $\sigma_i \sim 13$ km s $^{-1}$ – corresponding to thermal motion of a gas with $T \sim 10^4$ K – unlikely. However, both

- turbulent motion of the emitting gas (in the case of, e.g., Ly α production through fluorescence, Hogan & Weymann 1987; Mas-Ribas & Dijkstra 2016) and of cold gas relatively nearby the emitting source will lead to a broadening of the Ly α line prior to additional radiative transfer effects, and these larger σ_i values are relatively easy to justify. Interestingly, although even broader intrinsic lines of $\sigma_i \geq 400$ km s $^{-1}$ are allowed by the fitting pipeline (up to $\sigma_i \leq 800$ km s $^{-1}$), they are not favored by the data.
- The resulting (absorbing) dust optical depth of the shell-model is centered around $\tau_d \sim 2.45_{-0.41}^{+0.29}$. Within the geometry of the homogeneous shell, these values would correspond to extremely low escape fractions of $\sim 0.037_{-0.016}^{+0.028}$

which seem highly unlikely for the considered objects. Furthermore, if converted to a metallicity (using the SMC conversion factor of $Z/Z_{\odot} = 9.3 \times 10^{20} \text{ cm}^{-2}/N_{\text{HI}}\tau_{\text{d}}$ which assumes an albedo of $A = 0.32$, Pei 1992; Li & Draine 2001; Laursen et al. 2009) the resulting metallicities of $\log(Z/Z_{\odot}) = 2.5^{+0.93}_{-0.92}$ are unrealistically high.

Therefore, the literal interpretation of the dust optical depth is not very probable. However, as the uncertainty on the τ_{d} is mostly greater than unity (compare Fig. 3), lower dust contents are consistent with the spectral shape. The reason for these preferred large τ_{d} values can be understood when considering of how an increased dust optical depth changes the emergent Ly α spectrum. A common misconception – probably due to the (near-)frequency independence of the dust cross-section around $\lambda \approx 1216 \text{ \AA}$ (Pei 1992; Laursen et al. 2009) – is that the effect of dust does not change the Ly α spectrum (but merely the Ly α escape fraction). While this assumption holds for many cases, it does not universally. This is because dust attenuates the photons proportional to their path length through cold, dusty medium, and thus, if there is a correlation between emergent frequency and trajectory length, the shape of the spectrum will be changed. For instance, in “usual” double-peaked Ly α profiles through outflowing media (with an enhanced red side), the Ly α photons forming the blue peak have travelled further through neutral hydrogen. Therefore, an increased dust content will lower the blue peak and increase the spectral asymmetry. This might be the reason for the high τ_{d} preference of the data. However, for the observed spectra the blue side might be attenuated not by dust but by neutral gas in the CGM and/or IGM which scatters Ly α photons out of the line-of-sight, and thus, effectively absorb the blue side of the spectrum (Dijkstra et al. 2007; Laursen et al. 2011).

- The shell outflow velocities (i.e., $v_{\text{exp}} > 0$) are approximately normally distributed with mean $\sim 211 \text{ km s}^{-1}$ and standard deviation $\sim 94 \text{ km s}^{-1}$. For lower quality spectra (categories 1 and 2), we found also inflow velocities with similar magnitude. The values of v_{exp} thus agree with previous measured outflow velocities in the nearby (Kunth et al. 1998; Rivera-Thorsen et al. 2015) and distant Universe (Shapley et al. 2003; Kulas et al. 2012). Overall, we find (within $1-\sigma$) only $\sim 5\%$ of the spectra to be better fit by inflow velocities [$\sim 3\%$ of the confidence 3 spectra] and $\sim 25\%$ [$\sim 9\%$] to be consistent with inflows. These limits could potentially constrain the covering fraction of cold, inflowing gas and thus yield insights into the gas budget of high- z galaxies. We caution, however, that the directional dependence of Ly α spectra (in such scenarios) is yet unclear (see Fig. D.1 in Trebitsch et al. 2016, for an angle-averaged spectrum of an filamentary accreting object which shows signs of inflows).
- While not technically being a shell-model parameter, the redshift of the source is crucial for the fit. We display the redshift in Fig. 4 as shift between the Ly α peak z_{MW} (as provided by Herenz et al. 2017) and the modeled intrinsic redshift z . Furthermore, we convert the difference to velocity space resulting in

$$\Delta v = c \frac{z - z_{\text{MW}}}{1 + z_{\text{MW}}}. \quad (1)$$

We find Δv values of $\sim -76^{+79}_{-77} \text{ km s}^{-1}$ ($\sim -95^{+96}_{-78} \text{ km s}^{-1}$ for only the highest “confidence” spectra), which implies an emission blueward of the main spectral peak for the majority

of analyzed spectra – as commonly found for other Ly α emitting objects (e.g., Erb et al. 2014; Trainor et al. 2015). Only $\sim 3.8\%$ ($\sim 4.2\%$ of the “confidence” 3 spectra) of the spectra show $\Delta v > 0$ (above $1-\sigma$). On the other hand, $\sim 49\%$ of the spectra ($\sim 29\%$ of the “confidence” three spectra) are consistent with $\Delta z \sim 0$ (within $1-\sigma$). Another potentially interesting point is the correlation between N_{HI} and Δz , i.e., larger shifts for higher column densities which follows directly from the frequency diffusion in the models. Observationally, it has been established that this shift is anti-correlated with the Ly α equivalent width (Erb et al. 2014) which invites to the interpretation of facilitated Ly α escape in systems with less frequency diffusion.

Note that we did not find an evolution of any of the above discussed parameters with redshift. We found, however, that only spectra with high S/N (≥ 20) occupy the parameter space with $\Delta v \lesssim 200 \text{ km s}^{-1}$ or $N_{\text{HI}} \gtrsim 10^{19.5} \text{ cm}^{-2}$ – similarly to what we discussed above for v_{exp} . This is likely due to the fact that the spectral features required for, e.g., a large column density (for instance, the extended wing) is only apparent for higher quality spectra.

All the above described shell-model parameters, that is, the 16th, 50th, and 84th percentiles of the posterior distributions for each object are publicly available⁴.

3.3. Correlations with halo properties

The combined modeling of both the spectrum and surface brightness distribution is a crucial next step to understand how Ly α photons escape galaxies and what information they obtain on their trajectory as using both constraints breaks degeneracies which otherwise exist. Integral field spectrograph such as MUSE are the perfect tool to study these two angles simultaneously. As a first step towards the full joined modeling, we want to correlate the spectral with spatial information.

Included in the MUSE-Wide catalogue is the Kron (1980) radius R_{Kron} of each object as calculated by LSDcat (Herenz & Wisotzki 2017) as well as the flux within $\{1, 2, 3\} \times R_{\text{Kron}}$. LSDcat calculates R_{Kron} following the two-dimensional definition of Bertin & Arnouts (1996) which reads

$$R_{\text{Kron}} = \frac{\sum rI(r)}{\sum I(r)} \quad (2)$$

where the summations are carried out over the 2D pseudo-narrowband images created from the 3D MUSE datacubes.

Figure 5 shows the R_{Kron} (upper row), the flux within R_{Kron} (central row), and the ratio of the flux within $3R_{\text{Kron}}$ and R_{Kron} (lower row) versus the six shell-model parameters. The latter quantity is a measure how steep the surface brightness profile is falling off. In each panel, we also display the Spearman correlation coefficient. We cannot identify a clear correlation between the fitting parameters and the halo properties. However, some tentative correlations might be apparent. For instance, σ_i and the halo extent as well as the brightness of the source – in particular the high quality spectra (shown as red points) are somewhat correlated. Also Δv and the flux within R_{Kron} show some level of anti-correlation. In order to confirm or rule out these tentative correlations (as well as the ones discussed in Sect. 3.2), the uncertainty of the shell-model parameters should be lower than the correlation range of interest. This mean a similar number of spectra with better signal-to-noise ($S/N \geq 20$; cf. Fig. 3)

⁴ The full list is available at the CDS (see Appendix A). It is also available under <http://bit.ly/a-spectra-of-MW>

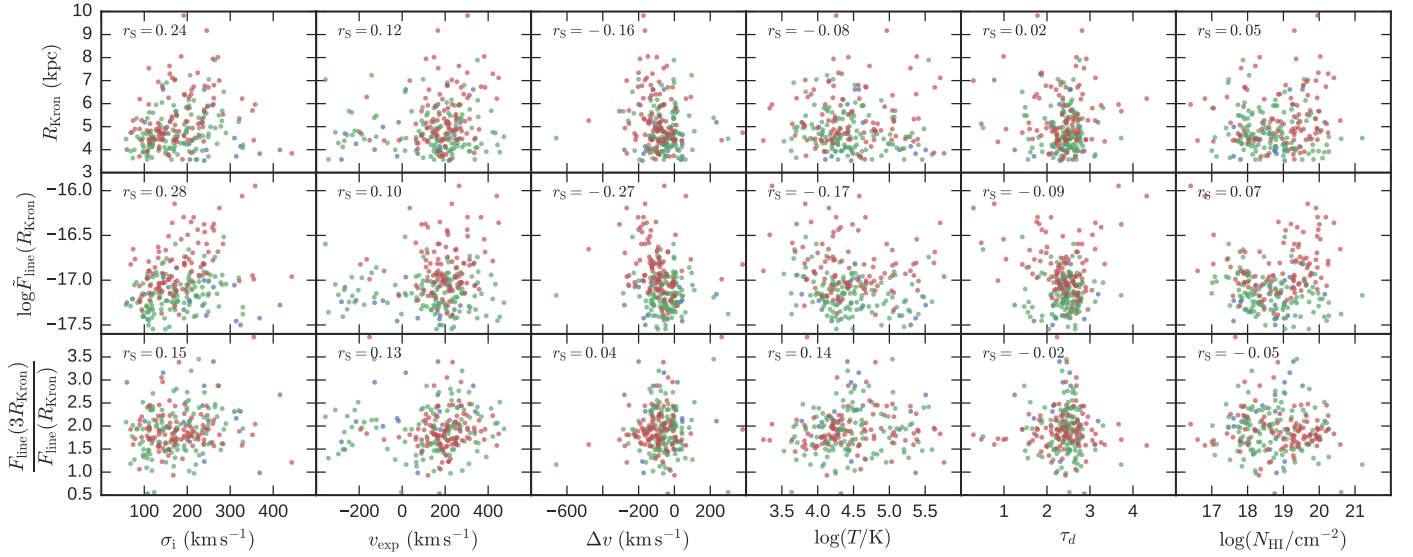


Fig. 5. Extent of the Ly α halo and its brightness versus the six obtained shell-model parameters. The *upper and central rows* show the Kron radius (in kpc) and the line flux (with $\bar{F} = F/(\text{erg s}^{-1} \text{ cm}^{-2})$) as a function of the fitting parameters (see Sect. 3.3 for more details). The *lower row* shows the flux ratio between $3\times$ and $1\times R_{\text{Kron}}$. The color coding corresponds again to the “confidence” category (blue, green, red in increasing order). Also shown in each panel are the Spearman correlation coefficients.

would be most useful – a goal which can be achieved in the near future given that this first release only covers about one fifth of the total survey area, and the “MUSE-Wide” scanning strategy is very shallow (one hour per field [Herenz et al. 2017](#)).

3.4. Contrasting the “shell-” with the “Gaussian-minus-Gaussian” model

As an alternative to the radiative-transfer based shell-model, we fit the 237 Ly α spectra using the a “Gaussian-minus-Gaussian” model (which has been previously used in the literature modeling Ly α spectra; e.g., [Jensen et al. 2013](#)). This model also consists of six free parameters, namely the location (i.e., the mean μ) and width (the standard deviation σ) of two normal distributions which have been scaled by an arbitrary amplitude (the total area under the curve A). Please note that in concordance with the name, we do not allow negative amplitudes (which could correspond to a “Gaussian-plus-Gaussian” model), and also don’t allow for negative fluxes, that is, we set the data point which would be negative to zero.

Figure 6 shows a comparison between the fit qualities of the two models using the $p(\chi^2)$ values of the best-fitting parameters. The color coding stands again for the “confidence” category assigned to each spectrum. Clearly, the shell-model can reproduce most spectra better than the (even simpler – but with the same number of free parameters) “Gaussian-minus-Gaussian” model leading to higher $p(\chi^2)$ values for $\sim 9\%$ of the spectra⁵. In particular, in some cases the “Gaussian-minus-Gaussian” model fails to reproduce the observed spectral shape completely (i.e., $p(\chi^2) \lesssim 0.1$) while the shell-model can fit same spectrum successfully. Overall, this improvement of the fit quality seems slightly larger for higher quality spectra (that is, higher “confidence” values); however, this trend is not statistically significant with the current data set. On the other hand, spectra that cannot be modeled using the shell-model can neither be reproduced

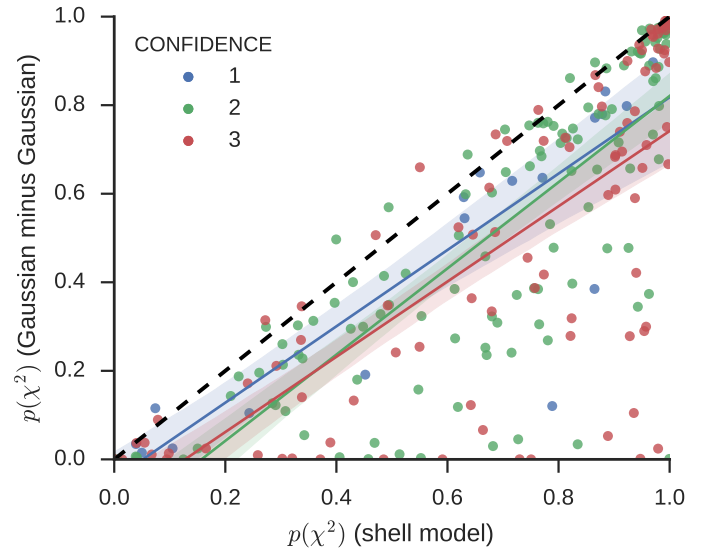


Fig. 6. Quality of the fits of the “shell” versus the “Gaussian-minus-Gaussian” models. The color stands for the three “confidence” categories. Also included (as a “guide to the eye”) are linear fits to the data, and the identity function (as black dashed line).

using the “Gaussian-minus-Gaussian” fit. Instead, both models yield comparable low $p(\chi^2)$ values.

Figure 7 illustrates the reason for superiority of the “shell-” over the “Gaussian-minus-Gaussian”-model. Each panel shows an observed Ly α spectrum (in blue), the best shell-model fit (in solid red with dotted red the intrinsic spectrum), and (in dashed green) the best “Gaussian-minus-Gaussian” fit. The two numbers in the top left and right corner of each panel show the $p(\chi^2)$ values of the best-fit shell-model and “Gaussian-minus-Gaussian” fit, respectively. This means, the leftmost panel of Fig. 7 shows an example where the shell-model yields a much better quality fit. The reason here is clearly the double peaked nature which cannot be captured by the “Gaussian-minus-Gaussian” model. The second panel from the left shows

⁵ Overall, 83% [52%] of the “Gaussian-minus-Gaussian” fits possess a $p(\chi^2) > 0.1$ [> 0.5].

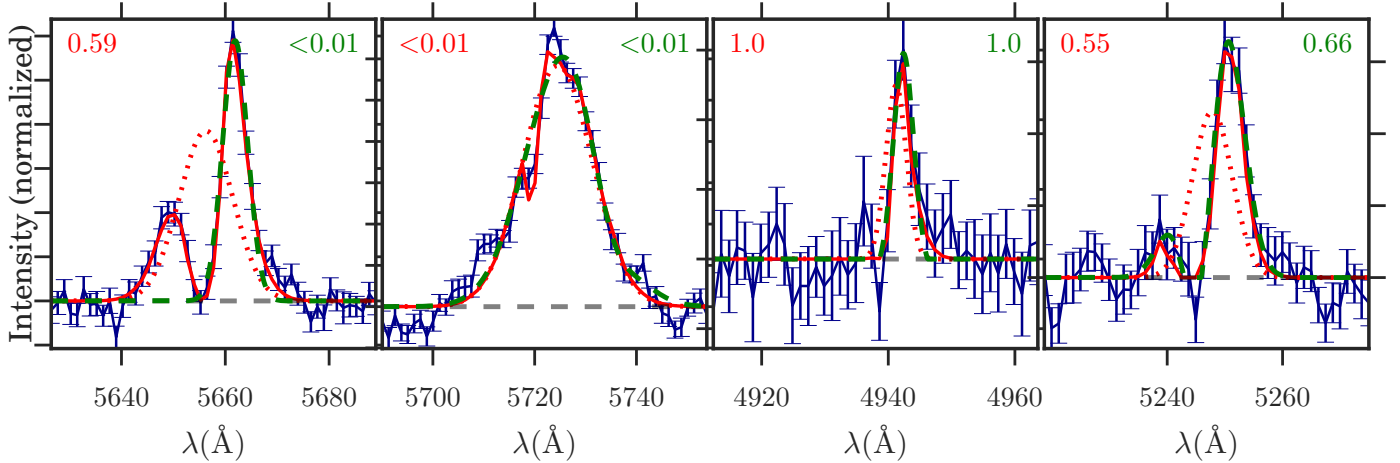


Fig. 7. Example spectral fits of the “shell” and “Gaussian-minus-Gaussian” models with all combinations of fitting failures/successes. The blue lines show the data, the red solid line the shell model fit (with the intrinsic spectrum as dotted red line), and the green dashed line shows the “Gaussian-minus-Gaussian” best fit. The numbers in the panel show the $p(\chi^2)$ values of the best fits in the corresponding colors.

the same spectrum as in Fig. 2, i.e., a case where the shell-model cannot reproduce the observed spectrum well. However, fitting two Gaussian curves yields a similar fit and, thus, also $p(\chi^2) < 0.01$. As mentioned in Sect. 3.1 the reason for these low $p(\chi^2)$ values in this case are the small error bars on the data combined with the slight negative flux bluewards of the line. It is noteworthy that such wide, relatively symmetric spectra can naturally be well reproduced using a simple Gaussian curve. This means per construction the “Gaussian-minus-Gaussian” model suits this spectral type well. However, also the shell-model can feature such a spectrum – given a low optical depth of the shell (through low column density and high outflow velocity) and a wide intrinsic spectrum. This will lead to hardly any radiative transfer effects, and thus, to a Gaussian emergent spectrum.

The third panel (from the left) in Fig. 7 displays an single-peaked, asymmetric spectrum. This is an example where both models yield good fits to the data. This is also the case in the right panel of Fig. 7 (which we chose because it is the spectrum where the $p(\chi^2)$ difference is greatest in favour for the “Gaussian-minus-Gaussian” model). Interestingly, here the two normal distributions can also reproduce the two peaks of the data. This is due to the lower blue peak (compared to the first panel) and the larger error within it.

A potential physical interpretation of the “Gaussian-minus-Gaussian” model is some intrinsic spectrum (e.g., shaped by within the interstellar medium) which is then processed by the circum- and/or intergalactic medium (see, e.g., Gronke & Dijkstra 2016; and Dijkstra et al. 2007, respectively). The latter step would lead to a “Ly α halo” surrounding the galaxy and – as (with increasing distance from the galaxy) most scatterings are out of the line-of-sight – can be modeled as an effective absorption. This would mean that an increased level of absorption should correlated positively with the halo size. However, we do not find any correlation of the “absorbed flux”⁶ ($r_S \approx -0.07$) with R_{Kron} . Neither we find any correlation with any other halo property discussed in Sect. 3.3. As both the intrinsic spectrum as well as the absorption feature may differ from a normal distribution – which makes the “Gaussian-minus-Gaussian” model a simplification – this result is maybe not too surprising.

⁶ We calculate the absorbed flux ratio as $F_{\text{abs}} = A_1 - \int f_{\text{GMG}}(\lambda)d\lambda$ where A_1 is the amplitude of the positive Gaussian, and $f_{\text{GMG}}(\lambda)$ is the best fit (normalized to unity).

One can surely extend the “Gaussian-minus-Gaussian” model with additional free parameters (by, e.g., allowing for negative amplitudes and non-zero skewness) in order to provide better fits to the observed Ly α spectra. However, one should keep in mind that the advantage of a radiative-transfer based model (such as the shell-model) is that its spectral shapes are at least a subset of all the possible Ly α spectra. This is not necessarily so for “more artificial” models. Also, these models to not directly alter the spectral shape by changing the frequency diffusion process, and, thus it physical content of the fitting parameters is even more questionable than in the shell-model.

4. Conclusions

We fitted the publicly available Ly α spectra of the “MUSE-Wide survey” published in Herenz et al. (2017) using the shell-model. This data-set contains 237 spectra around redshift $z \sim 3.8$. We carried out the fitting procedure using the pipeline described in (Gronke et al. 2015) which yields robustly the best-fit parameters as well as the respective confidence intervals. Our main findings can be described as follows:

- Overall, the shell-model provides excellent fits to a majority of the spectra (with >90% possessing a $p(\chi^2) > 0.1$; see Sect. 3.1) with a better fits than the ‘Gaussian-minus-Gaussian’ model (Sect. 3.4). Even the worst shell-model fits can reproduce the spectral shape reasonably well (cf. Fig. 2). This implies that this simple model can practically fit all 237 spectra.
- We identified common parameter ranges which are typical for observed spectra. This allows future studies to generate more realistic Ly α spectra, and to compare newly obtained shell-model parameters to this distribution. For this purpose, we make all the fits publicly available⁷. With the exception of the shell’s dust optical depth we find none of the parameters completely unphysical (see Sect. 3.2), i.e., within the range what has been derived by other means. For instance, we recovered from only the spectral shape outflows in the range of $\sim 200 \text{ km s}^{-1}$ (in particular, the higher quality spectra) which has been found using metal-absorption lines (e.g., Steidel et al. 2010).

⁷ The individual parameters are shown in Table A.1. It is also available at <http://bit.ly/a-spectra-of-MW>.

- Two recovered parameter distributions (which can have physical meaning in a multiphase medium with many clumps per sightline; see Gronke et al. 2017) are of particular interest: (i) the majority of spectra ($\sim 70\%$) are better fit through an outflowing shell and only $\sim 5\%$ are prefer an inflowing shell. Given firmer underlying data this could yield insights into the gas budget of high-redshift galaxies; (ii) half of the spectra can be fit with column densities of $N_{\text{HI}} \lesssim 10^{17} \text{ cm}^{-2}$. This suggests a possible large fraction of Lyman-continuum leakers in the MUSE-Wide data set and supports the importance of Ly α emitting galaxies on the ionizing budget (Dressler et al. 2015; Verhamme et al. 2015; Dijkstra et al. 2016b).
- We did not find any strong correlation neither amongst the shell-model parameters nor with the Ly α halo properties. However, a weak correlation between Δv and N_{HI} , and a tentative correlation between σ_1 and Δv exist.

This work serves also as a “proof-of-concept”, i.e., that the modeling of a large set of observed Ly α spectra – as will be common in the near future – is possible. A similar analysis can be improved by increasing the S/N of the spectra (cf. Fig. 3), and by providing priors on the systemic redshift (thus, confining Δv to values close to zero).

Acknowledgements. I thank the anonymous referee for constructive and helpful feedback. I am grateful to my PhD supervisor Mark Dijkstra for his guidance and comments on the draft. Furthermore, I thank Edmund Christian Herenz for a careful read of the draft. Also, I would like to thank him and the entire MUSE team for making the data used in this work publicly available. Finally, I wish to thank Lutz Wisotzki for inviting me to the Leibniz Institute for Astrophysics in Potsdam. This research made use of a number of open source software such as the Python programming language and its packages *astropy* (Astropy Collaboration et al. 2013), *IPython* (Pérez & Granger 2007), *matplotlib* (Hunter 2007), *seaborn* (Waskom et al. 2014), and *SciPy* (Jones et al. 2001).

References

- Adams, T. F. 1972, *ApJ*, 174, 439
- Ahn, S.-H., Lee, H.-W., & Lee, H. M. 2003, *MNRAS*, 340, 863
- Astropy Collaboration, Robitaille, T. P., Tollerud, E. J., et al. 2013, *A&A*, 558, A33
- Bacon, R., Accardo, M., Adjali, L., et al. 2010, in Ground-based and Airborne Instrumentation for Astronomy III, *Proc. SPIE*, 7735, 773508
- Bacon, R., Brinchmann, J., Richard, J., et al. 2015, *A&A*, 575, A75
- Barnes, L. A., Garel, T., & Kacprzak, G. G. 2014, *PASP*, 126, 969
- Bertin, E., & Arnouts, S. 1996, *A&AS*, 117, 393
- Bonilha, J. R. M., Ferch, R., Salpeter, E. E., Slater, G., & Noerdlinger, P. D. 1979, *ApJ*, 233, 649
- Cai, Z., Fan, X., Yang, Y., et al. 2016, *ApJ*, 837, 1
- Cantalupo, S., Arrigoni-Battaia, F., Prochaska, J. X., Hennawi, J. F., & Madau, P. 2014, *Nature*, 506, 63
- d’Agostino, R., & Pearson, E. S. 1973, *Biometrika*, 60, 613
- Dahle, H., Aghanim, N., Guennou, L., et al. 2016, *A&A*, 590, L4
- Dijkstra, M. 2014, *PASA*, 31, e040
- Dijkstra, M. 2017, ArXiv e-prints [arXiv:1704.03416]
- Dijkstra, M., Haiman, Z., & Spaans, M. 2006, *ApJ*, 649, 14
- Dijkstra, M., Lidz, A., & Wyithe, J. S. B. 2007, *MNRAS*, 377, 1175
- Dijkstra, M., Gronke, M., & Sobral, D. 2016a, *ApJ*, 823, 74
- Dijkstra, M., Gronke, M., & Venkatesan, A. 2016b, *ApJ*, 828, 71
- Drake, A. B., Guiderdoni, B., Blaizot, J., et al. 2017, *MNRAS*, 471, 267
- Dressler, A., Henry, A., Martin, C. L., et al. 2015, *ApJ*, 806, 19
- Erb, D. K., Steidel, C. C., Trainor, R. F., et al. 2014, *ApJ*, 795, 33
- Foreman-Mackey, D., Hogg, D. W., Lang, D., & Goodman, J. 2013, *PASP*, 125, 306
- Francis, P. J., Woodgate, B. E., Warren, S. J., et al. 1996, *ApJ*, 457, 490
- Fynbo, J. U., Møller, P., & Warren, S. J. 1999, *MNRAS*, 305, 849
- Goodman, J., & Weare, J. 2010, *Commun. Appl. Math. Comput. Sci.*, 5, 65
- Gronke, M., & Dijkstra, M. 2016, *ApJ*, 826, 14
- Gronke, M., Bull, P., & Dijkstra, M. 2015, *ApJ*, 812, 123
- Gronke, M., Dijkstra, M., McCourt, M., & Peng Oh, S. 2016, *ApJ*, 833, 1
- Gronke, M., Dijkstra, M., McCourt, M., & Oh, S. P. 2017, *A&A*, 607, A71
- Hansen, M., & Oh, S. P. 2006, *MNRAS*, 367, 979
- Hashimoto, T., Verhamme, A., Ouchi, M., et al. 2015, *ApJ*, 812, 157
- Hennawi, J. F., Prochaska, J. X., Cantalupo, S., & Arrigoni-Battaia, F. 2015, *Science*, 348, 779
- Herenz, E. C., & Wisotzki, L. 2017, *A&A*, 602, A111
- Herenz, E. C., Urrutia, T., Wisotzki, L., et al. 2017, *A&A*, 606, A12
- Hogan, C. J., & Weymann, R. J. 1987, *MNRAS*, 225, 1P
- Hunter, J. D. 2007, *Comput. Sci. Engin.*, 9, 90
- Jensen, H., Laursen, P., Mellema, G., et al. 2013, *MNRAS*, 428, 1366
- Jones, E., Oliphant, T., Peterson, P., et al. 2001, *SciPy: Open source scientific tools for Python*, <http://www.scipy.org/>
- Karman, W., Caputi, K. I., Caminha, G. B., et al. 2017, *A&A*, 599, A28
- Kron, R. G. 1980, *ApJS*, 43, 305
- Kulas, K. R., Shapley, A. E., Kollmeier, J. A., et al. 2012, *ApJ*, 745, 33
- Kunth, D., Mas-Hesse, J. M., Terlevich, E., et al. 1998, *A&A*, 334, 11
- Laursen, P., Sommer-Larsen, J., & Andersen, A. C. 2009, *ApJ*, 704, 1640
- Laursen, P., Sommer-Larsen, J., & Razoumov, A. O. 2011, *ApJ*, 728, 52
- Li, A., & Draine, B. T. 2001, *ApJ*, 554, 778
- Mas-Ribas, L., & Dijkstra, M. 2016, *ApJ*, 822, 1
- McCourt, M., Oh, S. P., O’Leary, R. M., & Madigan, A.-M. 2016, ArXiv e-prints [arXiv:1610.01164]
- McGreer, I. D., Clément, B., Mainali, R., et al. 2017, *MNRAS*, submitted [arXiv:1706.09428]
- Møller, P., & Warren, S. J. 1993, *A&A*, 270, 43
- Neufeld, D. A. 1990, *ApJ*, 350, 216
- North, P. L., Marino, R. A., Gorgoni, C., et al. 2017, *A&A*, 604, A23
- Osterbrock, D. E. 1962, *ApJ*, 135, 195
- Ouchi, M., Harikane, Y., Shibuya, T., et al. 2017, *PASJ*, submitted [arXiv:1704.07455]
- Partridge, R. B., & Peebles, P. J. E. 1967, *ApJ*, 147, 868
- Pearson, K. 1900, *The London, Edinburgh, and Dublin Philosophical Magazine and Journal of Science*, 50, 157
- Pei, Y. C. 1992, *ApJ*, 395, 130
- Pérez, F., & Granger, B. E. 2007, *Comput. Sci. Engin.*, 9, 21
- Planck Collaboration, Ade, P. A. R., Aghanim, N., et al. 2016, *A&A*, 594, A13
- Powell, M. J. 1994, in *Advances in Optimization and Numerical Analysis* (Springer), 51
- Rhoads, J. E., Malhotra, S., Dey, A., et al. 2000, *ApJ*, 545, L85
- Rivera-Thorsen, T. E., Hayes, M., Östlin, G., et al. 2015, *ApJ*, 805, 14
- Schaerer, D., Hayes, M., Verhamme, A., & Teyssier, R. 2011, *A&A*, 531, A12
- Shapley, A. E., Steidel, C. C., Pettini, M., & Adelberger, K. L. 2003, *ApJ*, 58, 65
- Sobral, D., Matthee, J., Darvish, B., et al. 2015, *ApJ*, 808, 139
- Steidel, C. C., Adelberger, K. L., Shapley, A. E., et al. 2000, *ApJ*, 532, 170
- Steidel, C. C., Erb, D. K., Shapley, A. E., et al. 2010, *ApJ*, 717, 289
- Trainor, R. F., Steidel, C. C., Strom, A. L., & Rudie, G. C. 2015, *ApJ*, 809, 89
- Trebtsch, M., Verhamme, A., Blaizot, J., & Rosdahl, J. 2016, *A&A*, 593, A122
- Vanzella, E., De Barros, S., Cupani, G., et al. 2016, *ApJ*, 821, L27
- Verhamme, A., Schaerer, D., & Maselli, A. 2006, *A&A*, 460, 397
- Verhamme, A., Schaerer, D., Atek, H., & Tapken, C. 2008, *A&A*, 491, 26
- Verhamme, A., Dubois, Y., Blaizot, J., et al. 2012, *A&A*, 546, A111
- Verhamme, A., Orlitová, I., Schaerer, D., & Hayes, M. 2015, *A&A*, 578, A7
- Verhamme, A., Orlitová, I., Schaerer, D., et al. 2017, *A&A*, 597, A13
- Waskom, M., Botvinnik, O., Hobson, P., et al. 2014, *seaborn: v0.5.0* (November 2014), <https://doi.org/10.5281/zenodo.12710>
- Wisotzki, L., Bacon, R., Blaizot, J., et al. 2016, *A&A*, 587, A98
- Yang, H., Malhotra, S., Gronke, M., et al. 2016, *ApJ*, 820, 130
- Yang, H., Malhotra, S., Gronke, M., et al. 2017, *ApJ*, 844, 171

Appendix A: Table of shell-model parameters

Table A.1 shows the retrieved shell-model parameters, the MUSE UNIQUE ID (Herenz et al. 2017), and the $p(\chi^2)$ values of the best-fit. In this table, we use (as in the rest of this work) the notation A_c^b where A denotes the median and b (c) the difference to the 16th and 84th percentile.

Note that the full version of Table A.1 is available at the CDS and under <http://bit.ly/a-spectra-of-MW>

Table A.1. Retrieved shell-model parameters alongside with the MUSE UNIQUE ID and the $p(\chi^2)$ value of the best-fit.

UNIQUE ID	σ_i (km s ⁻¹)	v_{exp} (km s ⁻¹)	Δv (km s ⁻¹)	$\log(T/\text{K})$	τ_d	$\log(N_{\text{HI}}/\text{cm}^{-2})$	$p(\chi^2)$
101005016	209 ⁺⁵³ ₋₄₃	279 ⁺¹²⁴ ₋₇₈	-87 ⁺⁷³ ₋₁₀₆	4.4 ^{+0.9} _{-1.1}	2.4 ^{+1.7} _{-1.6}	18.1 ^{+1.3} _{-1.6}	0.83
101009024	310 ⁺⁵⁸ ₋₇₁	340 ⁺¹⁰² ₋₁₃₇	-127 ⁺¹¹¹ ₋₁₀₃	4.23 ^{+0.86} _{-0.99}	2.4 ^{+1.7} _{-1.7}	18.2 ^{+1.1} _{-1.7}	0.63
101010025	278 ⁺⁴⁷ ₋₅₅	181 ⁺¹⁰⁹ ₋₃₆₈	-108 ⁺²²³ ₋₉₄	4.4 ^{+0.8} _{-1.1}	2.2 ^{+1.8} _{-1.6}	18.9 ^{+0.9} _{-1.8}	0.31
101011026	175 ⁺²⁵ ₋₁₄	-120 ⁺²⁵ ₋₁₃	82 ⁺¹⁴ ₋₂₇	3.83 ^{+0.48} _{-0.61}	1.5 ^{+2.1} _{-1.2}	17.79 ^{+0.71} _{-0.99}	0.04
101012027	145 ⁺³⁹ ₋₃₀	216 ⁺⁹⁷ ₋₆₃	-79 ⁺⁷⁰ ₋₁₁₁	4.3 ^{+1.0} _{-1.0}	2.2 ^{+1.8} _{-1.6}	19.34 ^{+0.60} _{-0.81}	0.98
101015031	211 ⁺³⁸ ₋₅₈	190 ⁺¹³² ₋₄₉	-124 ⁺⁶⁹ ₋₇₇	4.8 ^{+0.6} _{-1.4}	2.4 ^{+1.7} _{-1.7}	19.3 ^{+0.6} _{-1.2}	0.9
101016032	186 ⁺⁴¹ ₋₃₄	382 ⁺⁵⁶ ₋₇₀	-148 ⁺⁵² ₋₅₂	5.4 ^{+0.5} _{-1.7}	0.99 ^{+1.70} _{-0.77}	20.03 ^{+0.38} _{-0.39}	0.34
101023043	172 ⁺³³ ₋₂₄	277 ⁺¹²⁶ ₋₉₀	-7.7 ^{+45.3} _{-95.2}	4.4 ^{+1.3} _{-1.0}	2.6 ^{+1.6} _{-1.7}	17.9 ^{+1.6} _{-1.4}	0.82
101024044	213 ⁺¹¹ ₋₁₁	117 ⁺³¹ ₋₄₁	-277 ⁺⁶⁵ ₋₅₆	4.00 ^{+0.75} _{-0.75}	2.0 ^{+1.9} _{-1.2}	19.94 ^{+0.31} _{-0.24}	0.96
101025045	169 ⁺⁵³ ₋₅₁	176 ⁺¹⁸² ₋₈₉	-119 ⁺¹²⁸ ₋₁₅₀	4.20 ^{+1.04} _{-0.99}	2.7 ^{+1.6} _{-1.7}	19.4 ^{+0.7} _{-1.6}	0.99

Notes. The full version of the table is available at the CDS.